

SUPPLEMENTARY MATERIALS

Phase flows in state spaces

The time course of state variables is prescribed by dynamic systems, often represented by differential or integral-differential equations as in the case of the Epileptor. The time series resulting from solving differential equations can either be plotted as the value of the state variables over time, or equivalently as a trajectory in the state space. The state space (also sometimes referred to as phase space) is spanned by the state variables and a trajectory is a connected path through phase space. As an approximation, the trajectory may also be represented in a space spanned by its delayed coordinates (Takens 1981) (see Supplemental Figure 3). Such visualization unfolds the trajectory if the dimension of the delay space corresponds to at least $2n+1$ times the dimension of the attractor or flow in the original state space. Then there is a topological mapping from the original state space to the embedding space. The delay time for the attractor reconstruction from a scalar time series of infinite length can be chosen almost arbitrarily (Buzug and Pfister 1992). The time derivative of the state variables gives the instantaneous rate of change of the system and defines a tangent vector in the state space, basically indicating how the system will evolve along the trajectory. The tangent vector is a vector at every point in state space, which is equivalent to the solution of the evolution equation at that point. Essentially at each point in the state space there exists a vector defining a vector field, which describes the directed flow through the state space embodying the evolution equation. Hence a trajectory traces the time-dependent solution of a dynamical system through a succession of instantaneous states.

Bifurcations and invariances

As control parameters of a dynamic system change, the structure of the flow in state space will also depend on these parameters. If a state variable is sufficiently slower than all other state variables (as in the case of the Epileptor), then the slow variable can be also regarded as acting as a control parameter for finite periods of time. Small changes in the slow parameter or control parameters may then produce no qualitative changes in the state space until a critical value is reached and the dynamical system is said to have gone through a bifurcation. In the neighborhood of a hyperbolic fixed point (where all eigenvalues from a linearization around the fixed point are non-zero), the Hartman–Grobman theorem states that the behavior of a dynamical system is invariant and qualitatively the same as the behavior of its linearization near this point provided that no eigenvalue of the linearization has its real part equal to 0. Therefore when dealing with such fixed points one can use the simpler linearization of the system to analyze its behavior.

Sufficiently close to the critical control parameter value of a local bifurcation (i.e. when an equilibrium point changes its stability), a dynamical system may be mapped upon a nonlinear canonical form of a given bifurcation via a coordinate transform (Kuznetsov 1998), which defines the normal form of the dynamical system. Global bifurcations occur when 'larger' invariant sets, such as periodic orbits, collide with equilibria. This causes changes in the topology of the trajectories in the phase space, which cannot be confined to a small neighborhood, as is the case with local bifurcations. Normal forms of global bifurcations are not systematically defined. Bifurcations show characteristic scalings of their amplitudes and frequencies as a function of the control parameter and its difference to its critical value (Izhikevich, 2000). Further away from this critical parameter value, structural stability remains a fundamental property of a dynamical

system, which means that the qualitative behavior of the trajectories represented by the topology of the flow in state space is unaffected by small (sufficiently smooth) parameter variations. Examples of such qualitative properties are numbers of fixed points and periodic orbits (but not their periods). This behavior holds for all systems in two dimensions, but is more difficult to generalize for higher dimensions where more complex behaviors may be more typical such as strange attractors and hence need to be studied on a case-by-case basis.

Alternative formulation of Epileptor equations

The low-pass filtering effects of the integral $g(x)$ can be rewritten through the use of a dummy variable u . Then the Epileptor equations read as follows:

$$\begin{aligned}\dot{x}_1 &= y_1 - f_1(x_1, x_2) - z + I_{rest1} \\ \dot{y}_1 &= y_0 - 5x_1^2 - y_1 \\ \dot{z} &= \frac{1}{\tau_0}(4(x_1 - x_0) - z) \\ \dot{x}_2 &= -y_2 + x_2 - x_2^3 + I_{rest2} + 2u - 0.3(z - 3.5) \\ \dot{y}_2 &= \frac{1}{\tau_2}(-y_2 + f_2(x_2)) \\ \dot{u} &= -\gamma(u - 0.1x_1)\end{aligned}$$

All parameters and functions are as in the main text. The dummy variable u acts as a low pass filter due to the time scale separation: $\frac{1}{\gamma} = 100 \gg \tau_2$.

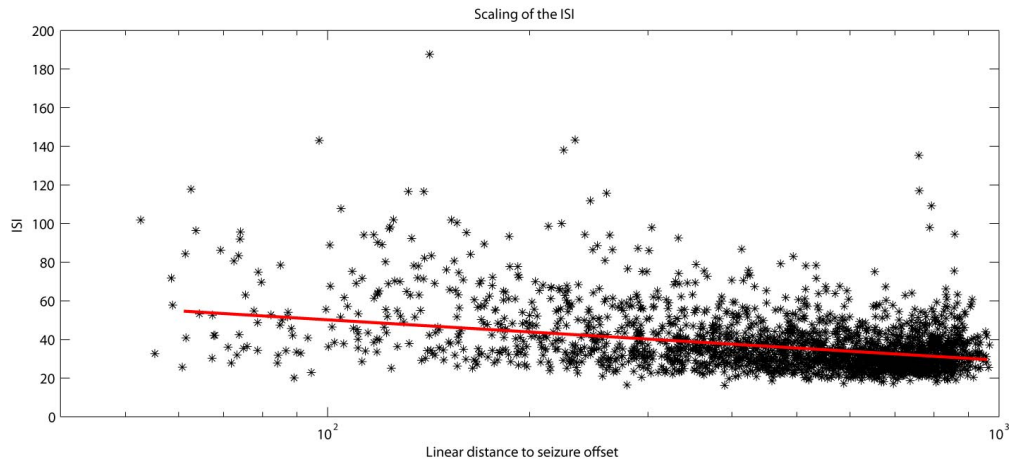
Assessing logarithmic scaling in interspike intervals

We assessed the best model for our data using a sample of 20 seizures (16 mouse, 2 zebrafish, 2 human) via goodness-of-fit (GoF) with sum of squared residual error (SSE) and degree-of-freedom-adjusted R-square (R^2). Several potential equations were tested: $\log(\text{Interspike interval (ISI)}) = a \cdot \log x + b$, power law ($a \cdot x^b + c$), inverse square root

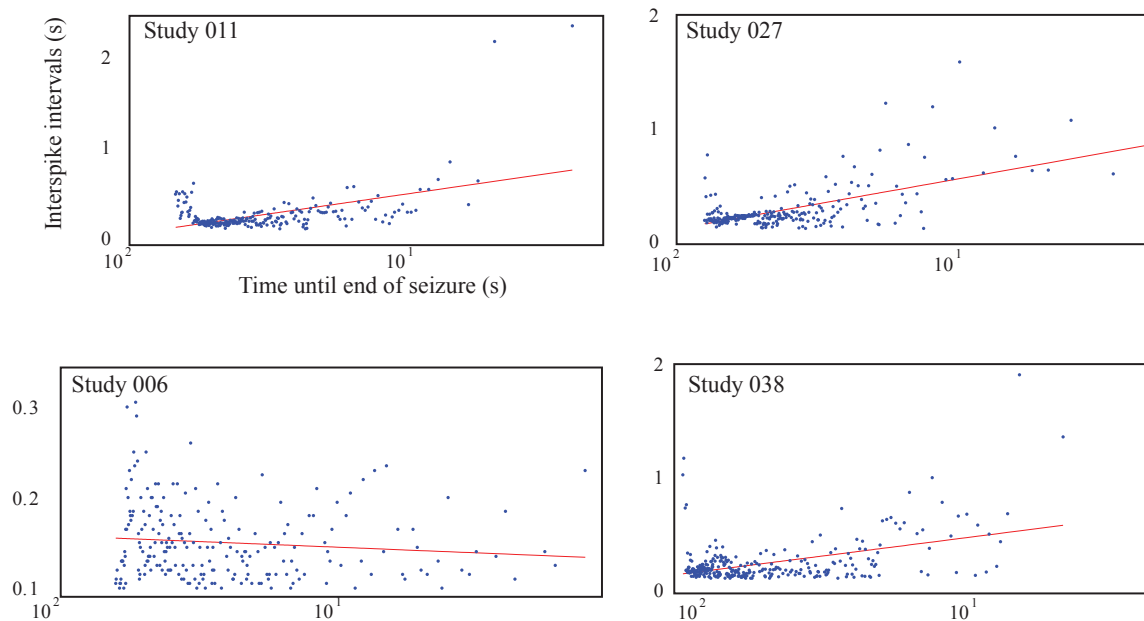
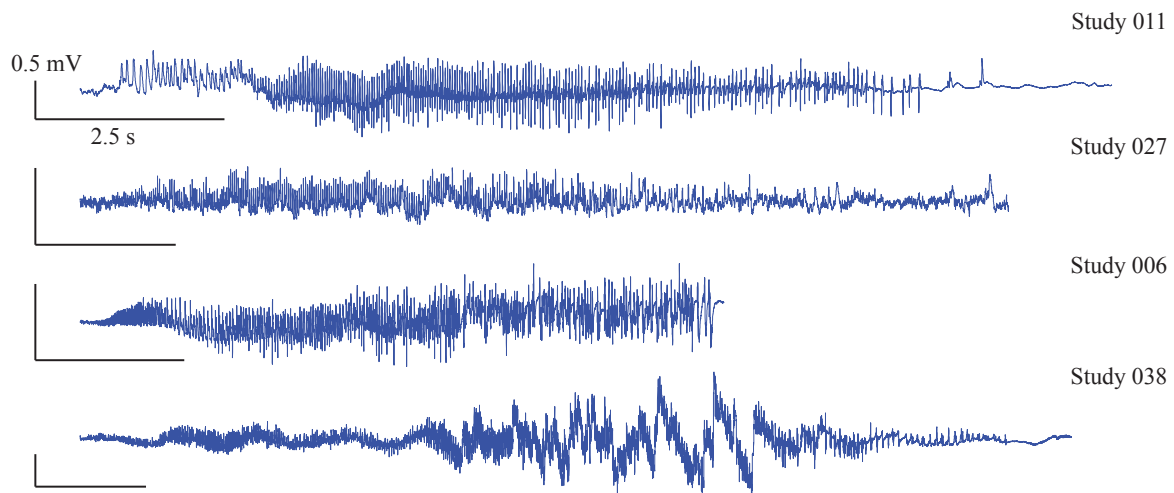
$(a/\sqrt{x} + b)$ and exponential $(a \cdot \exp(b \cdot x))$. Choice of best fit was made by comparing the GoF with a qualitative assessment of how each equation captured the dynamics. We used the R-square to compare GoF between the different equations, reinforced by the fact that all equations have the same number of predictors (degrees of freedom). We also considered the constant model ($ISI = k$); however this was clearly not preferred in any of the training data because the variable x was significant in all of them.

Qualitatively, the equation must predict that interspike intervals increase as the seizure terminates and then spiking stops completely-the “critical slowing down” that has been previously identified (Kramer et al., 2012). Exponential equations were rejected because they underestimated the ISI near the end of seizures and predicted that spikes would continue after the seizure ended. Linear, constant, and polynomial functions also did not capture the dynamics near seizure termination. Thus, power law (of which inverse square root is a special case) and log equations are the primary candidates, but often are quite similar in this range of data. In cases where GoF from log and power law were similar, we performed a modified predicted residual sum of squares (PRESS) statistic (Tarpey, 2000) to predict the entire distribution of ISI by fitting from data in only the last 25% of the seizure. The GoF was then assessed by calculating the SSE with that predicted model extrapolated to the entire dataset. We compared power law with log scaling in 20 seizures (16 mouse, 2 zebrafish, 2 human) and found log scaling to have lower RMSE in 16 of the cases ($p < 0.005$, binomial test) and concluded that log scaling is the most appropriate model (Supplemental Figure 9A). When these equations were tested on the whole cohort of human patients, there were some data that did not fit any of the equations well. A small number of the human seizures (4 out of 24) did not slow down at the end, producing “reversed” slopes (Supplemental Table 1, Supplemental Figure 2C). Note that clinically this type of seizure

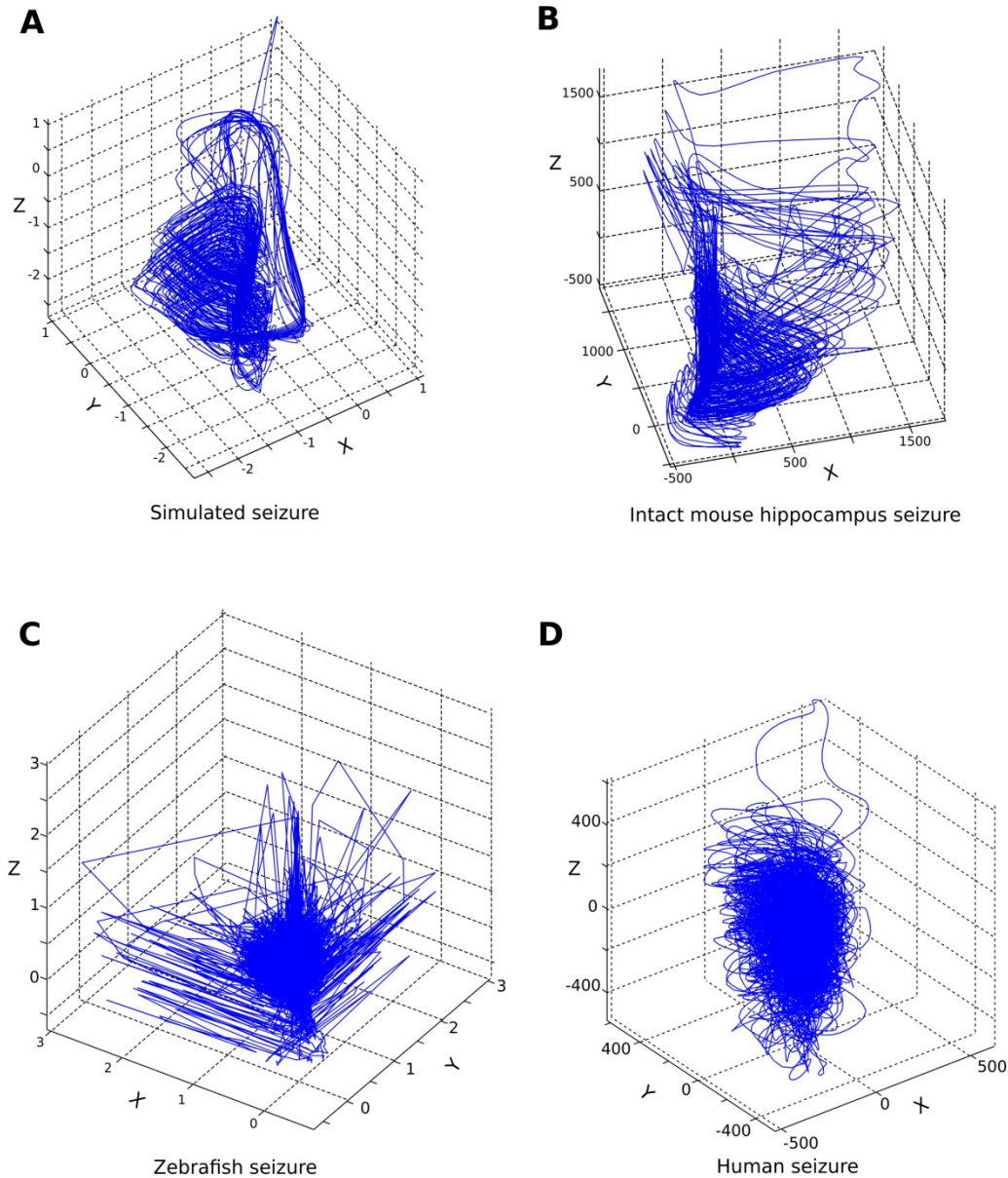
is very unusual, as ‘slowing down’ is a well-known characteristic of human seizure termination. Interestingly, the ISI for these 4 patients was adequately modeled with a constant, which places them into a different class of the seizure taxonomy in Table 1. There were two other effects occasionally seen in all species that were not explained by the log scaling. The first was irregular, slow firing at seizure onset (e.g. Fig. 6A). This “stuttering” was usually large spike wave discharges occurring before the fast spiking, in the period in which seizure onset is difficult to define. These types of seizure onset have also recently been identified in a heuristic classification of seizure types (Perucca et al. 2013). To be conservative, these periods were included within the seizure epoch, though clinicians typically disagree about the precise time of seizure onset (Benbadis et al., 2009). The second was clonic firing at the end of seizure. The fast spiking during clonic bursts was similar to that at the beginning of the seizure, while the intervals between bursts fit the log scaling (Fig. 6D, Supplemental Figure 9). When we compared inverse square root and log scaling in the full complement of 24 human seizures (Supplemental Table 1), the R^2 , SSE and PRESS values were not significantly different, and thus we deemed either the SNIC ($1/\text{square root}$) or the homoclinic (log) bifurcations the most appropriate. Including the DC shift to the bistability of the offset, we conclude that the homoclinic bifurcation is correct for the seizures we studied.



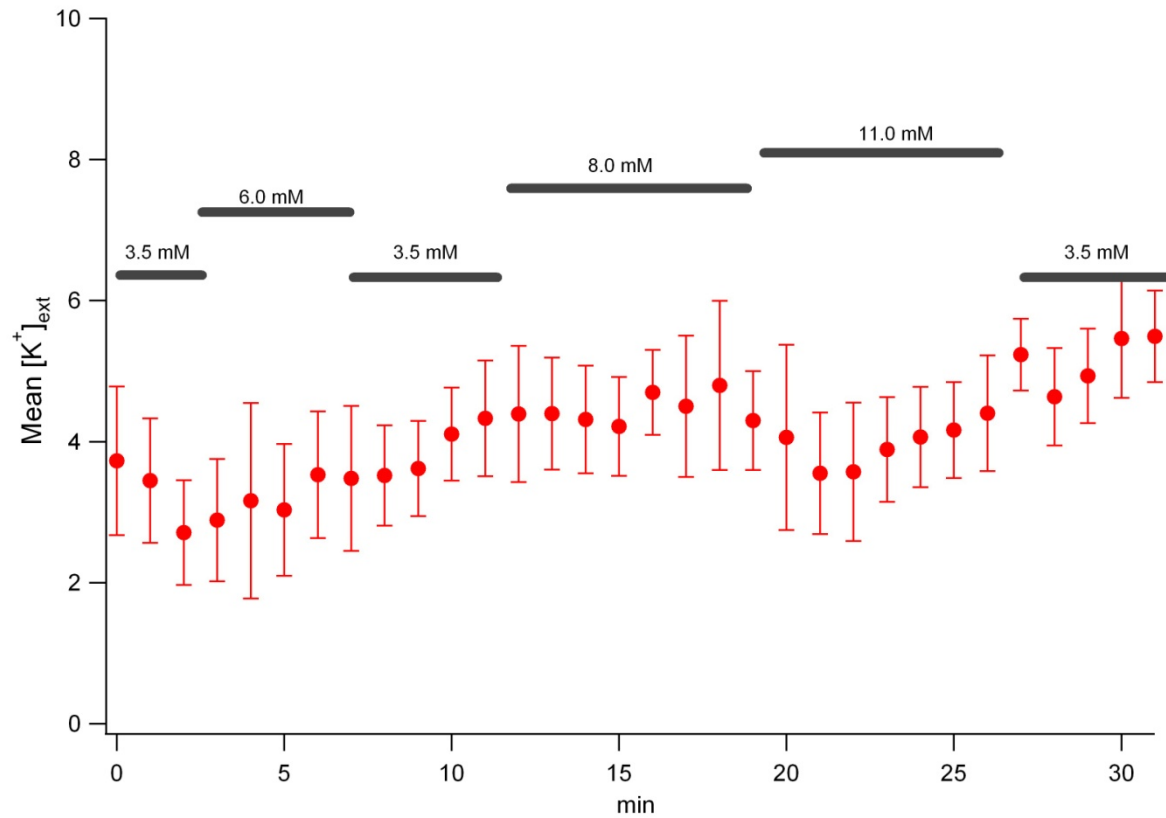
Supplemental Figure 1: Logarithmic scaling of interspike interval (ISI) in the Epileptor model, providing evidence for a homoclinic bifurcation at seizure offset.



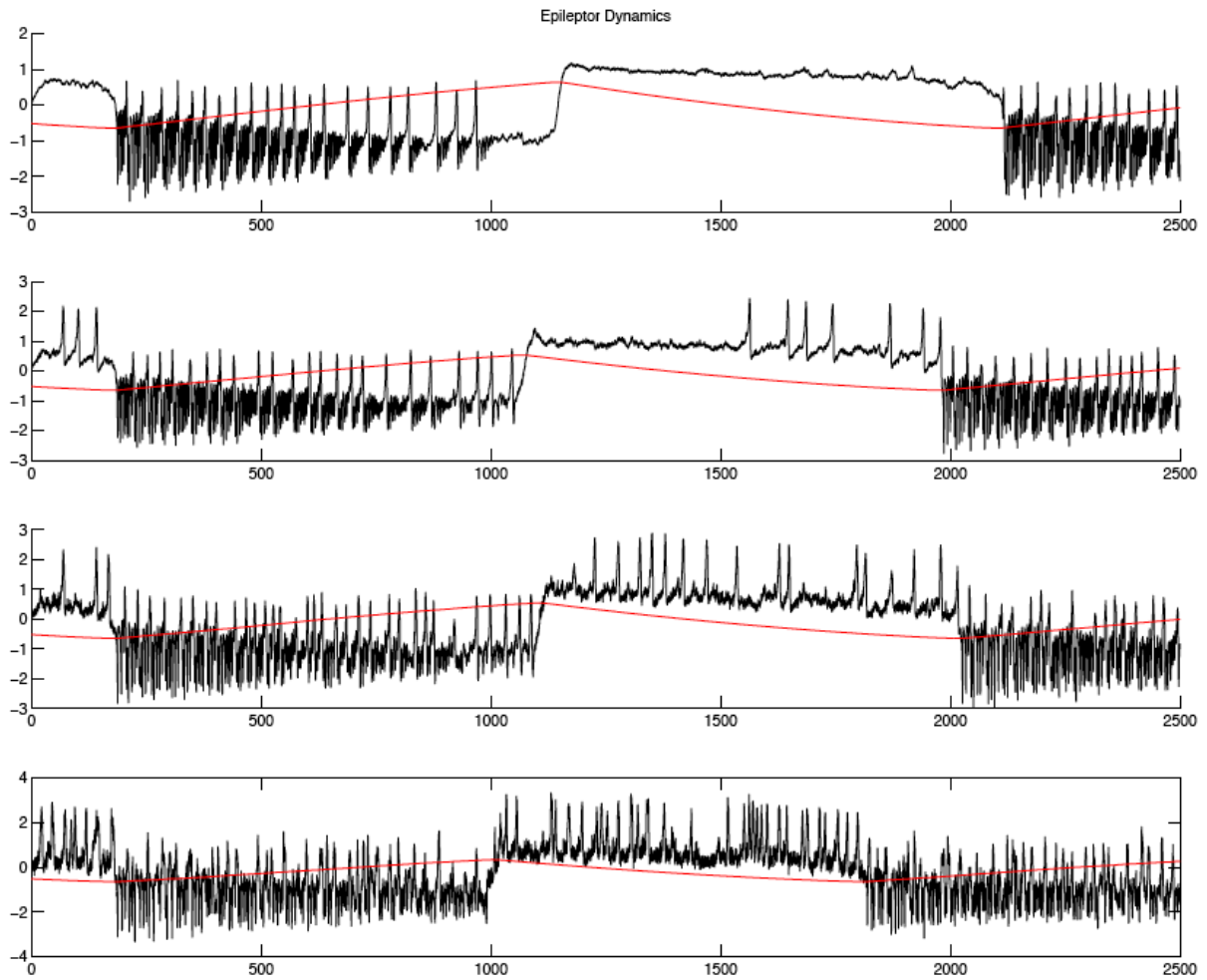
Supplemental Figure 2: Examples from four of the human patients listed in Suppl. Table 1. Top: raw data from one EEG channel. Bottom: Interspike intervals as a function of time to end of seizure. Red line: data fit to log equation. Note that in study 006, the ISI are much smaller than in other patients and do not slow down at the end of the seizure: the data do not fit well to the log equation and could potentially be modeled as a constant.



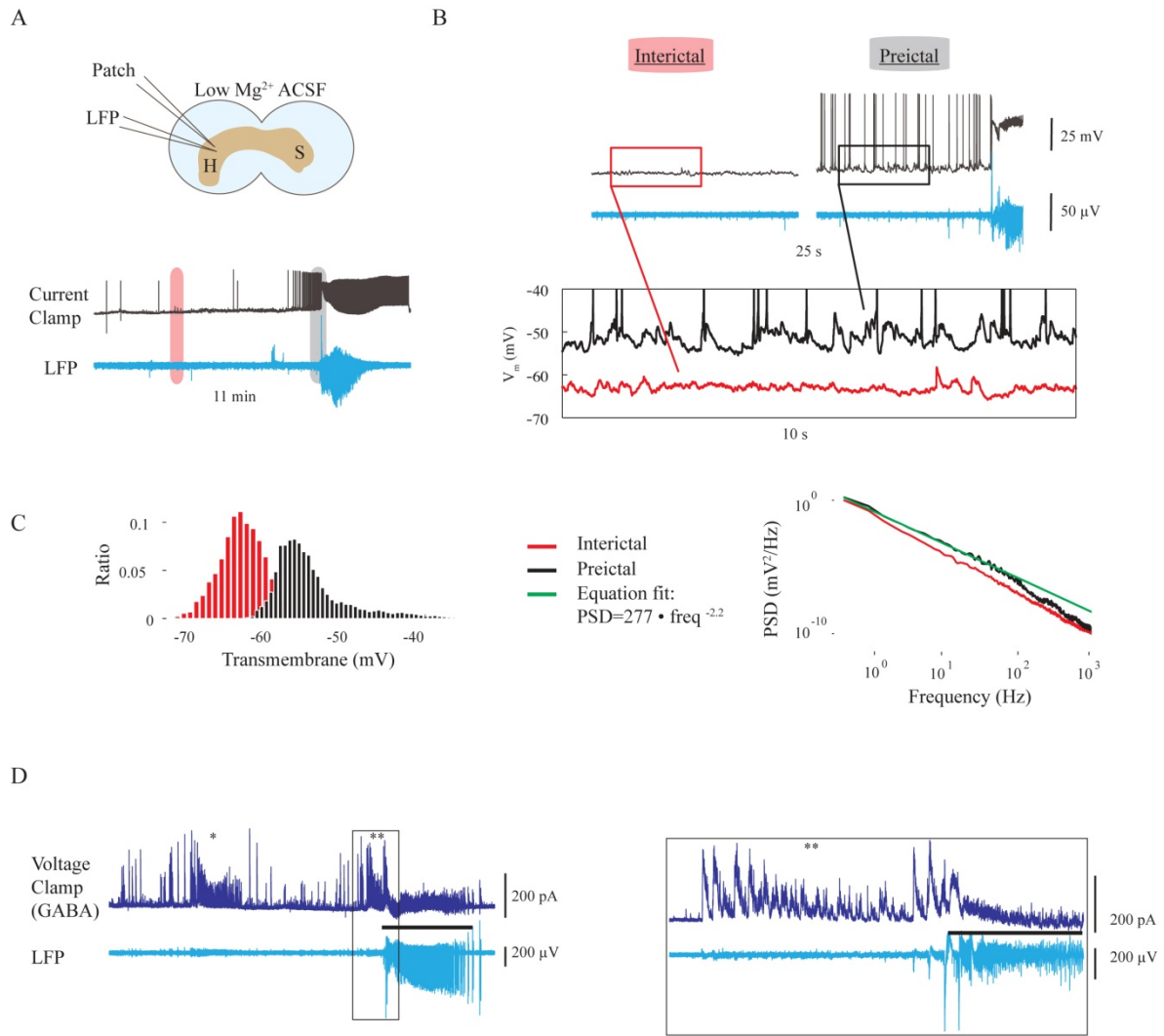
Supplemental Figure 3. Topologies of seizures in various species. Delayed plot representation of seizures generated in Epileptor (A), in the intact mouse hippocampus (B), zebrafish (C) and human (D), corresponding to the examples shown in Fig. 1. In this space, the coordinates of a point $M(X,Y,Z)$ are $x(t)$ (the value of the field potential at time t), $x(t-\Delta t)$ and $x(t-2\Delta t)$; with Δt a small time interval. The trajectories, although distorted, are very similar in nature, composed of spirals traveling on cone-like structures.



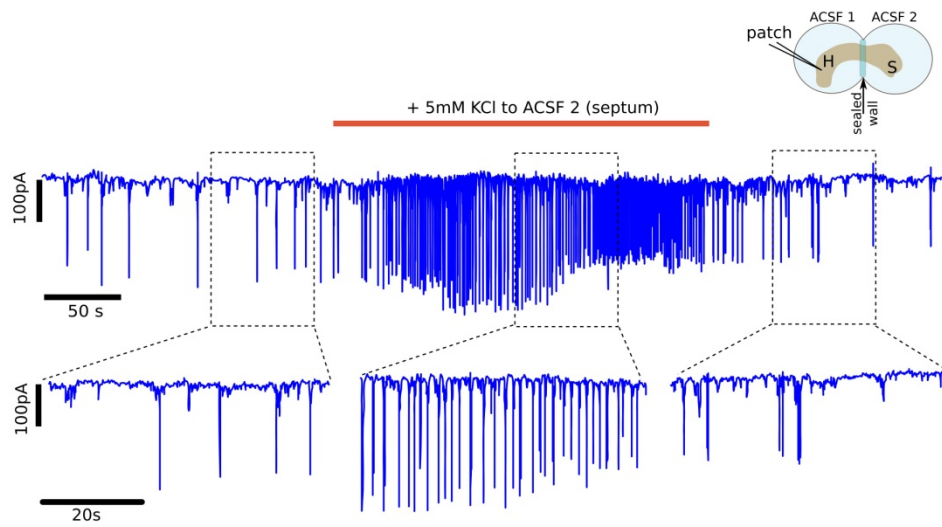
Supplemental Figure 4. Lack of crosstalk between the chambers containing the hippocampus and the septum. Extracellular $[K^+]_{ext}$ was raised in the septum chamber (horizontal bars), and the extracellular $[K^+]_{ext}$ measured with a K^+ sensitive electrode in the chamber with the hippocampus. Raising $[K^+]_{ext}$ in the septum chamber did not change $[K^+]_{ext}$ in the hippocampus. The experiment was reproduced in 3 different preparations.



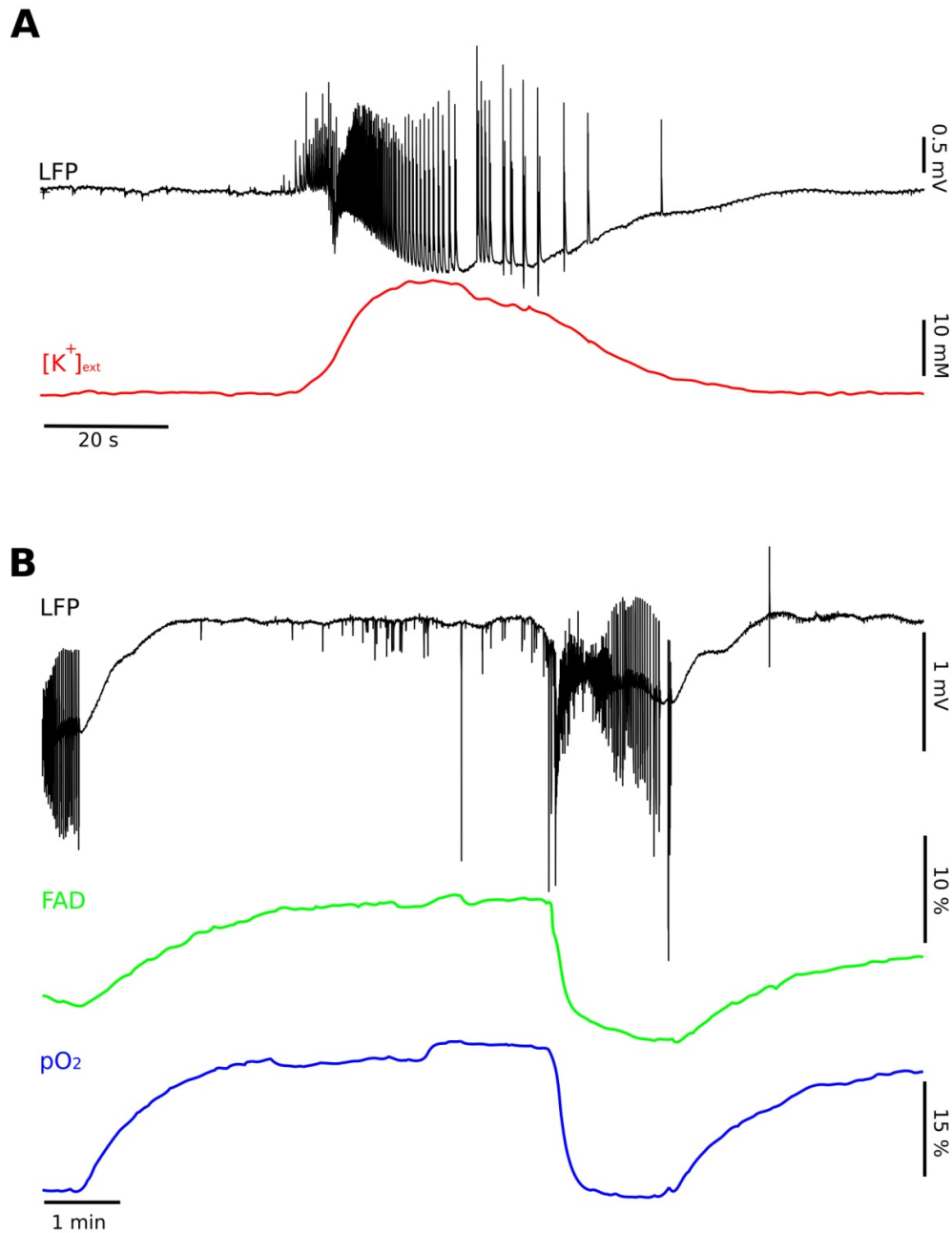
Supplemental Figure 5. Different seizure-like events generated by the Epileptor in the presence of increasing levels of noise, from top to bottom. The initial conditions for the numerical simulation are $x_1=0.022$; $y_1=0.91$; $z=3.84$; $x_2=-1.11$; $y_2=0.73$. Noise is introduced into each equation as linear additive Gaussian white noise with zero mean and a variance of 0.025 for the first subsystem and 0.1, 0.25, 0.71, and 1 (from top to bottom) for the second subsystem. Although noise changes the some aspects of the appearance, the main building blocks, fast discharges and SWEs, are still present albeit organized differently.



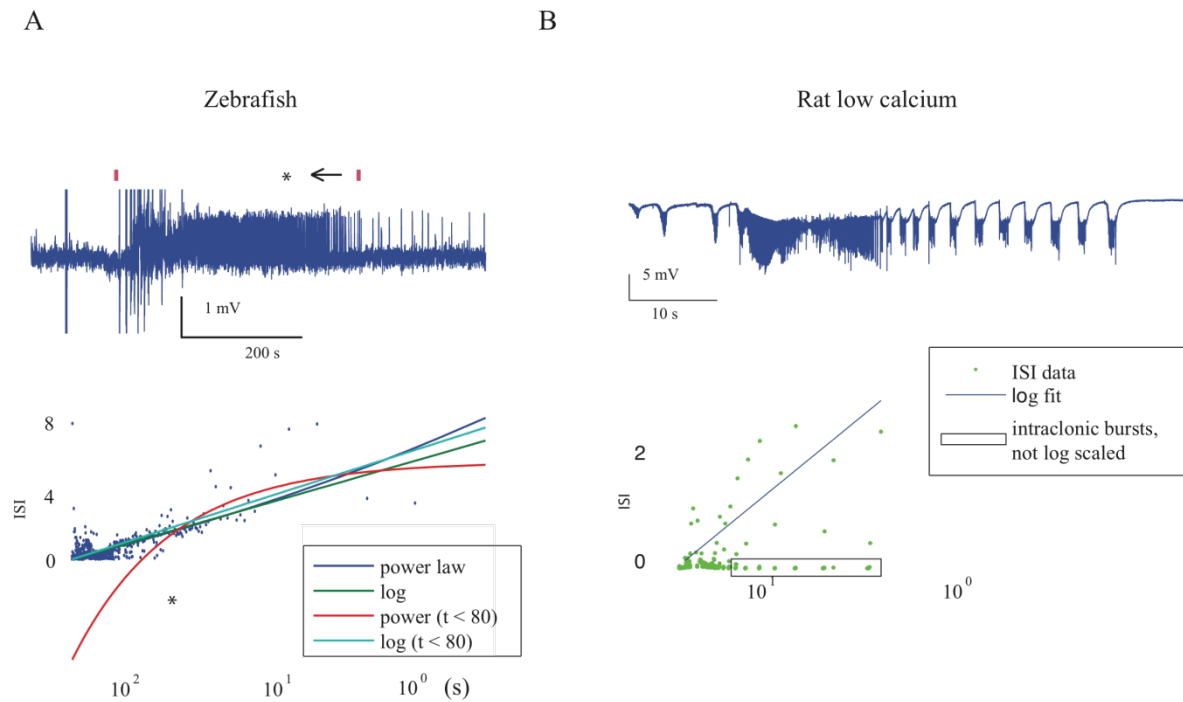
Supplemental Figure 6: Increase of synaptic noise at seizure onset in the hippocampus in low Mg^{2+} . **A.** An Oriens-Lacunosum Moleculare (O-LM) GABAergic neuron was recorded in whole cell configuration current clamp mode simultaneously with the local field potential (LFP) in low Mg^{2+} conditions. **B.** Zoom of the activities in the orange (interictal, i.e. far from the SLE) and grey (pre-ictal, just before SLE onset) regions shown in **A**. During the interictal period, few synaptic inputs could be detected (red trace). In contrast, during the preictal period, there was strong barrage of synaptic inputs, leading to cell firing (black trace). Note that the preictal period was associated with a 10 mV depolarization of the membrane. The same behavior was found in four other GABA neurons (four different preparations). **C.** Left: Histogram of membrane voltages in preictal vs. interictal period. Both are Gaussian distributions, and the preictal period has a higher mean (net depolarization). Right: Comparison of power spectral density (PSD) between preictal and interictal. Both have a “pink” noise spectrum, but with a clear difference in the two periods (see Supplemental Table 1). **D.** Simultaneous recordings of LFP and of a Hippocampal-Septum GABA neuron in whole cell configuration voltage clamp mode at +10 mV to measure spontaneous postsynaptic inhibitory (GABAergic) currents (IPSCs). Note the strong increase in GABAergic activity (*), which was not associated with any detectable activity in the LFP. Just before SLE, there was another barrage of activity (**, and inset). Similar increases in noise were found in 20 other GABA neurons (20 different preparations).



Supplemental Figure 7: Increasing $[K^+]$ in the septum compartment increases synaptic activity in a simultaneously-recorded neuron in the hippocampus. The ACSF of the hippocampal compartment was normal. Here, we used a Cs-Cl solution, with which glutamatergic, cholinergic and GABAergic inputs appear as downward deflections. Note the increase in synaptic activity as soon as the septum is exposed to increased $[K^+]$. Upon wash out, synaptic activity returned to baseline values. With this dual chamber, there is no crosstalk (leakage) between one chamber and the other (Supplemental Figure 5). The experiment was reproduced in three different preparations.



Supplemental Figure 8. Extracellular $[K^+]_{ext}$, FAD and O_2 share a time course similar to that of the slow state variable. A. Simultaneous recording of the field potential (top trace) and extracellular $[K^+]_{ext}$ during an SLE. Note that the time evolution of $[K^+]_{ext}$ mirrors that of the DC shift of the field. B. Simultaneous recording of FAD and O_2 levels during SLEs. Interestingly, it is only when FAD and O_2 levels return to baseline that a new SLE can occur, similar to the predicted behavior of the slow state variable. The experiment was reproduced in $n=10$ preparations for $[K^+]_{ext}$ measurements and $n=3$ preparations for FAD/ O_2 .



Supplemental Figure 9: Logarithmic scaling. A: Comparison of log scaling and power law. With the majority of data near the beginning of the seizure (high x), power and log are sometimes very similar. However, if the equations are fit to only the last 25% of the data (t=0 to 80, 33/635 points) and extrapolated, the log fit still represents the data well, while the power law does not. Asterisks: T=80. B: During SLE in rat hippocampal slices caused by very low calcium, the interspike intervals exhibit log scaling. There were prominent clonic bursts of fast activity at the end. Box: clonic fast spiking intervals ignored during equation fit.

| Study | Gender | Age | Location | Pathology | R ² |
|-------|--------|-----|--------------------|------------------------------|----------------|
| 4_2 | F | 27 | R Temp-Occ | Neocortical gliosis | 0.062 |
| 5 | M | 26 | R Temp-Hippoc | MTS | 0.344 |
| 6 | M | 25 | L Front | Not resected | 0.007* § |
| 10 | F | 13 | L Front-Par | Neocortical gliosis | 0.140 |
| 11 | F | 34 | R Front | FCD IIB | 0.252 § |
| 12_2 | M | 37 | R, L Temp | Gliosis | 0.076 |
| 16 | F | 36 | R Temp | Remote leptomeningitis | 0.058 |
| 17 | M | 39 | R Temp-Hippoc | MTS | 0.101 |
| 19 | M | 33 | L Temp | Neocortical gliosis | 0.144 |
| 20 | M | 10 | R Front | Hemorrhagic stroke | 0.138 |
| 21 | M | 16 | R Front | Neocortical gliosis | 0.018 |
| 22 | F | 21 | L Temp | Neocortical gliosis | 0.573 |
| 23 | M | 16 | L Occ | Remote destructive injury | 0.053 |
| 24 | F | 23 | L,R Front-Par-Temp | Not resected | 0.322 |
| 26 | M | 9 | L Front-Temp | Neocortical gliosis, FCD IIB | 0.010* |
| 27 | F | 34 | L Temp | MTS | 0.377 § |
| 29 | F | 22 | L Temp | MTS and neocortical gliosis | 0.001 |
| 30 | F | 18 | L Front | Remote vascular injury | 0.060 |
| 31 | M | 5 | R Front | FCD IIA | 0.279 |
| 33 | M | 3 | L Front | Cortical tuber | 0.003* |
| 34 | F | 33 | R Front | Grade 2 oligodendroglioma | 0.018 |
| 37 | F | 62 | R Par | Not resected | 0.105 |
| 38 | M | 58 | L Temp | MTS | 0.207 § |
| 40 | M | 32 | L Front-Par | Not resected | 0.038* |

Supplemental Table 1: Patient summary and goodness-of-fit

Deidentified data for each individual patient are stored on www.ieeg.org as a numbered “Study #” (e.g. “4_2” is “Study 004_2”). EEG, demographic, and clinical metadata are all freely available from the website. All studies present in the database at time of analysis were included except for one that had no data (Study 014) and one that had no seizure (Study 028). Pathology listed is taken from the clinical documentation. *- indicates data that did not fit the log equation well and resulted in a “reversed” slope.

§- Subject data shown in Figure S5. Study 24 was used in Fig. 3. Study 34 was used for Fig. 1 and Suppl. Fig. 4 & 6D. R²: DoF-adjusted R² of logarithmic equation fit (perfect fit = 1). Temp: temporal lobe, Occ: occipital, Front: frontal, Par: parietal, Hippoc: hippocampus, MTS: mesial temporal sclerosis, FCD: focal cortical dysplasia.

| | Noise/N | V_m Noise Ratio | Peak noise intensity | LFP Ratio | Time to event (s) |
|----------------------|------------|-----------------------|-------------------------------|--------------|-------------------|
| Spont 0 Mg^{2+} CC | 2/2 (2) | 4.2 ± 1.3 | 301 mV ² | $1.3 \pm .4$ | 105 ± 35 |
| Spont 0 Mg^{2+} VC | 10/16 (16) | 2.7 ± 2 | 98040 pA ² | $1.1 \pm .2$ | 35 ± 21 |
| Spont 0 Mg^{2+} AP | 6/13 (13) | 54 ± 68 (AP rate) | | | 26 ± 18 |
| Summary 0 Mg^{2+} | 18/31 (31) | | | | 33 ± 35 |
| Evoked KCl VC | 4/9 (5) | 3.3 ± 3.5 | 51898 pA ² | $1 \pm .1$ | 200 ± 135 |
| Evoked mannitol VC | 2/5 (3) | 2.9 ± 4.1 | 4548 (144580) pA ² | $1 \pm .2$ | 172 ± 176 |

| Noise Parameters | | | | |
|----------------------|---------------|------------------|----------------|--------------|
| | K | Baseline change | Ratio # spikes | Distribution |
| Spont 0 Mg^{2+} VC | 1.3 ± 0.2 | 28 ± 31 (pA) | 1.4 ± 0.8 | lognormal |
| Spont 0 Mg^{2+} CC | 1.9 ± 0.3 | 6 ± 2.7 (mV) | 2.9 ± 0.6 | lognormal |
| Evoked KCl | 1.4 ± 0.2 | 30 ± 26 (pA) | 2 ± 2.3 | lognormal |
| Evoked mannitol | 2.1 ± 0.2 | 29 ± 29 (pA) | 1.1 ± 1.1 | Gumbel |

Noise/N= number of experiments with increased noise/total experiments. Parenthesis= total number of seizures; V_m noise ratio= preictal/interictal noise intensity. This and all subsequent columns only measure those bursts with increased noise; Peak noise intensity= maximum preictal value of noise intensity in 100 ms windows; LFP ratio= preictal/interictal variance of field potential; Time to event= time prior to seizure that noise began; K= parameter in $1/\text{frequency}^k$ equation fit in power spectrum; Baseline change= preictal-interictal median value; Ratio # events= preictal/interictal total spikes; Distribution= best fit of interspike intervals.

Supplemental Table 2: Noise analysis. Top: in 0 magnesium bursting, synaptic noise increases over 50% of the time, often over a minute prior to the burst. This change is often not measureable in field potential electrodes. Similarly, loose-attached electrodes see an increase in firing rate prior to the bursts. Similar results were obtained when evoking seizures with either additional potassium or mannitol, however the mannitol did not increase synaptic noise significantly. Bottom: noise had similar characteristics in the zero magnesium and KCl-evoked models, with lognormally distributed, frequent spike times. The mannitol evoked seizures had very different spike distributions: less frequent and associated with large LFP spikes, fitting the Gumbel (extreme value) distribution.

Supplemental references

Benbadis SR, LaFrance WC Jr., Papandonatos GD, Korabathina K, Lin K, Kraemer HC. Interrater reliability of EEG-video monitoring. *Neurology* 73, 843-846, 2009

Buzug T, Pfister G. Optimal delay time and embedding dimension for delay-time coordinates by analysis of the global static and local dynamical behavior of strange attractors. *Phys Rev A* 45, 10, 7073-7084, 1992.

Izhikevich EM . Neural Excitability, Spiking, and Bursting. *International Journal of Bifurcation and Chaos* 10, 1171-1266, 2000.

Kantz H, Schreiber T. *Nonlinear time series analysis* (Cambridge University press, Cambridge), 1997.

Kramer MA, Truccolo W, Eden UT, Lepage KQ, Hochberg LR, Eskandar EN, et al. Human seizures self-terminate across spatial scales via a critical transition. *Proc Natl Acad Sci USA*. 109(51):21116-21, 2012.

Merrill DR, Bikson M, Jefferys JG. Electrical stimulation of excitable tissue: design of efficacious and safe protocols. *Journal of neuroscience methods*. 141(2):171-98, 2005.

Perucca P, Dubeau F, Gotman J. Intracranial electroencephalographic seizure-onset patterns: effect of underlying pathology. *Brain*. 2013.

Takens F. Detecting strange attractors in turbulence. In D. A. Rand and L.-S. Young. *Dynamical Systems and Turbulence*, Lecture Notes in Mathematics, vol. 898. Springer-Verlag. pp. 366–381. 1981.

Tallgren P, Vanhatalo S, Kaila K, Voipio J. Evaluation of commercially available electrodes and gels for recording of slow EEG potentials. *Clin Neurophysiol.* ;116(4):799-806, 2005.

Tarpey T. A Note on the Predicted Sum of Squares Statistic for Restricted Least Squares. *The American Statistician* 54, 116-118, 2000.